IEEE Access
Multidisciplinary | Rapid Review | Open Access Journal

Received July 18, 2019, accepted September 10, 2019, date of publication September 16, 2019,
date of current version September 30, 2019.

*Digital Object Identifier 10.1109/ACCESS.2019.2941447*

# Design and Analysis of a Five-Phase Fault-Tolerant Permanent Magnet Synchronous Motor for Aerospace Starter-Generator System

**YIGUANG CHEN AND BO LIU**
School of Electrical and Information Engineering, Tianjin University, Tianjin 300072, China
Corresponding author: Yiguang Chen (chenyiguang@tju.edu.cn)

This work was supported by the National Natural Science Foundation of China under Grant 51377114.

**ABSTRACT** In this paper, a novel five-phase fault-tolerant permanent magnet synchronous motor (FTPMSM) is designed for aerospace starter-generator (SG) system. Small teeth are placed at the center of the slots, in which the two coils belong to different phases, and on both sides of the small teeth, thermal insulation materials are placed. In this way, the motor owns low thermal coupling and no electromagnetic coupling among different windings. By optimizing the stator size and rotor structure, the short-circuit current is limited to a low level and thus the motor has strong fault-tolerant capability under short-circuit fault. The finite element analysis (FEA) model of the five-phase FTPMSM is established, by which no-load characteristic, load characteristic, and fault-tolerant capability of the motor are analyzed. The simulation results show that the mutual inductance of different phase windings are almost zero, and the motor has good fault-tolerant capability. Finally, the prototype of the proposed five-phase FTPMSM is built to verify the design and simulation results.

**INDEX TERMS** Starter-generator, fault-tolerant, finite element analysis, permanent magnet synchronous motor.

## I. INTRODUCTION

Nowadays, with the development of power electronics technology and aerospace technology, as the main secondary energy, electric energy has gradually replaced the traditional hydraulic energy and gas energy in aerospace field [1], [2]. Compared with hydraulic energy and gas energy, electric energy is easier to realize automation, integration, intellectualization, and lightweight in the field of transmission and management. The SG system combines a starting system and power supply in one power unit that can be used as a starter or a generator. In traditional starting system and power supply system, two independent motors are needed. One is a starter to drive the engine, the other is a generator to supply power. By contrast, only one motor is used in SG system, which can operate in motor or generation mode. Therefore, SG system has the advantages of small size, light weight and high efficiency [3].

The associate editor coordinating the review of this manuscript and approving it for publication was Jiansong Liu.

As the main component of the SG system, the motor plays a vital role in its performance. The motor used in SG system needs to satisfy many requirements: simple structure, high reliability, high conversion efficiency, high power density, and high torque density. Various types of motors have been employed in the SG system. In [4], a detailed description of the requirements for motors used in the aerospace field was given, including weight, volume, efficiency, fault-tolerant capability, torque density, speed range and torque ripple. In [5], a switched reluctance motor with 6 stator poles and 4 rotor poles was designed for the aircraft SG system. The system was rated at 30 kW, 270V DC and capable of meeting variable speed operation. The switched reluctance motor was mounted to the gas turbine engine shaft, operated in both motor mode, from zero to 26,000 r/min, and generate mode covering a speed range from 27,000 r/min to 46,850 r/min. In [6], a SG system for automobile applications with 42-V power net was described. This system was based on an induction machine which was directly mounted on the engine crankshaft and controlled using the technique of direct

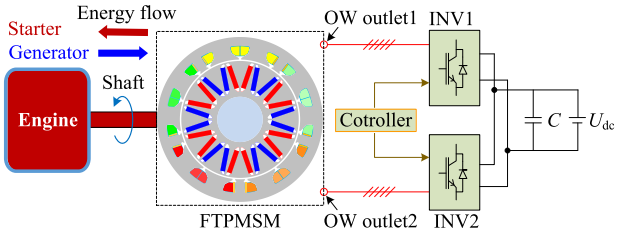


**FIGURE 1.** The SG system topology of the five-phase FTPMSM.

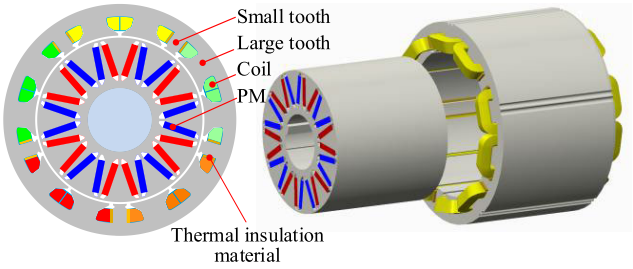


**FIGURE 2.** The configuration of the five-phase FTPMSM.

torque control. In [7], a SG system based on the wound-rotor synchronous machine was discussed. In order to achieve constant field current for the main generator, this paper proposed three detailed excitation control methods and achieved the expected result.

Due to the inherent advantages of high power density, high operation efficiency, simple structure, and simple control, the PMSM has drawn more and more attentions and recognitions in the SG system [8]–[12]. Multiphase motor owns the advantages of large power output with low DC voltage supply, low torque ripple, good fault tolerant ability, which has been investigated in [13], [14]. Therefore, multiphase motor can be an alternative choice over conventional three-phase motor in the SG system.

This paper proposes a five-phase FTPMSM for the SG system of rocket liquid oxygen engine. The PMSM used in aircraft SG mostly adopts Y connection, while the open ended winding (OW) is adopted in the proposed motor. The open ended winding scheme can improve the utilization of DC voltage, so that under certain DC voltage supply, the motor can achieve higher speed at rated current, which would increase power density of the system. Meanwhile, as the five-phase windings become electrical isolated, the fault-tolerant capability of the motor is improved. The SG system topology is shown in Fig. 1. The system employs two inverters. In the first stage, the motor operates in motor mode, powered by batteries, to start the engine from zero to 2000 r/min. The two inverters are operated in the inverter state, and the electric energy of the battery is converted into mechanical energy of the engine through the motor. Then, the motor operates in generator mode, driven by the engine, to supply power for thrust vectoring nozzle servo system of rocket and charge the batteries. The two inverters work in the controlled rectifier state, and the direction of current flow and electromagnetic torque is opposite to that of the motor mode, i.e., the mechanical energy of the engine is converted into electric energy through the motor. When the motor operates as a generator, speed range of the engine driving the motor is from 3500 r/min to 5000 r/min. The controller of the SG system can control the motor to operate in either motor mode or generation mode.

## II. STRUCTURE OF THE PROPOSED FTPMSM

The proposed five-phase FTPMSM is evolved from the conventional fractional-slot concentrated-winding (FSCW) 10-slot/12-pole five-phase PMSM. Fig. 2 shows the topology of the proposed motor. Each phase winding of the conventional 10-slot/12-pole five-phase PMSM consists of two sets of coils that are wound in alternate directions, which can eliminate armature reaction mutual inductance. However, owing to the coil edges of two-phase adjacent windings are in the same slot, the slot leakage mutual inductance exists. Based on the conventional structure, the small teeth are added at the center of stator slots, as shown in Fig. 2. Due to the exist of small teeth, the slot leakage flux of coils closes through the nearby small teeth instead of the coils of other phase windings, which makes slot leakage mutual inductance almost zero. Therefore, the mutual inductance of the motor is almost zero, which improves the fault-tolerant capability. The thermal insulation materials are placed on both sides of small teeth to reduce thermal coupling between adjacent two-phase windings [15], [16].

As the motor is surrounded by liquid oxygen, the ambient temperature is low, about −183°C. The resistance of coils is very small in this environment, which makes the copper loss small, and iron loss becomes the main part of the total loss. In order to reduce iron loss, the stator teeth and yoke are designed wide and the slot area is small. The motor adopts interior permanent magnet (IPM) with V-shape rotor structure to limit short-circuit current, reduce the loss of PM, and prevent them from irreversible demagnetization [17].

In order to verify that the five-phase FTPMSM has no mutual inductance, taking phase A as example, the magnetomotive force (MMF) is analyzed. Based on the assumption that only air-gap MMF exists, and the current in the slot is concentrated at the center line of the slot. Fig. 3(a) shows the MMF distribution along the circumference of air-gap under normal condition. It can be seen that the air-gap MMFs below the coils of other four-phase windings are zero, thus the magnetic fluxes of other four-phase windings are zero. Fig. 3(b) shows the MMF distribution along the circumference of air-gap under coil-1 with inter-turn short-circuit fault condition. It can be seen that the air-gap MMFs below the coils of other four-phase windings are same. Since two sets coils of each phase winding are wound in alternate directions, the magnetic fluxes of other four-phase windings are also zero. The conclusion is also applicable to MMF generated by other four-phase currents.

In order to further verify that the motor has no mutual inductance, the 2D FEA model is established. The PMs are removed from the FEA model, thus the magnetic field is only

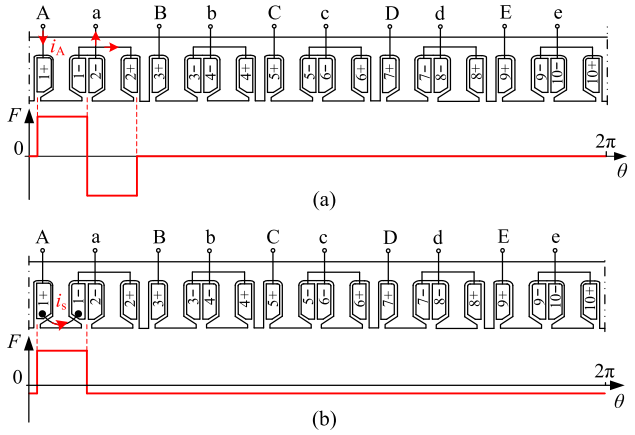


**FIGURE 3.** The MMF distribution diagram of phase A winding. (a) Under normal conditions. (b) Under a set of coils with short-circuit fault condition.

generated by exciting current. Fig. 4(a) and (b) show flux lines distribution of the motor when two sets of phase A coils are input d-axis and q-axis exciting current, respectively. It can be observed that the slot leakage flux lines of coils close through the nearby small teeth and no flux lines pass through the other four-phase windings. Fig. 4(c) and (d) show flux lines distribution of the motor when only one set of phase A coils is input d-axis and q-axis exciting current. It can be observed that the numbers of flux lines passing through the coils of other four-phase windings are almost equal, and the magnetic fluxes of other four-phase windings are also zero because two sets of coils of each phase winding are wound in alternate directions. The conclusion is also applicable to the case of other four-phase windings with exciting current. Therefore, it is verified that the added small teeth make the mutual inductance almost zero, which improves the fault-tolerant capability of the motor.

## III. DESIGN OF THE PROPOSED FTPMSM

### A. OPTIMIZATION OF THE SMALL TEETH ANGLE

The stator structure is illustrated in Fig. 5, where $\kappa$ is mechanical angle of the small tooth. It can be seen that the mechanical angle of two adjacent large teeth is $36° - 0.5\kappa$, such as large tooth 1 and 2, and the mechanical angle of two large teeth separated by a small tooth is $36° + 0.5\kappa$, such as large tooth 2 and 3.

Since the magnetic field of permanent magnets is symmetrical, the magnetic field only contains odd harmonics. Therefore, the harmonic order $v$ of EMF can be expressed as

$$v = 2k + 1 \quad k = 0, 1, 2, \cdots \tag{1}$$

The winding pitch coefficient $k_{yv}$, winding distribution coefficient $k_{qv}$, and winding coefficient $k_{\mathrm{w}v}$ of $v$ order harmonic can be expressed as follows

$$k_{yv} = \sin v\left(\frac{216° - 3\kappa}{2}\right) = \cos v\left(18° - \frac{3\kappa}{2}\right) \tag{2}$$

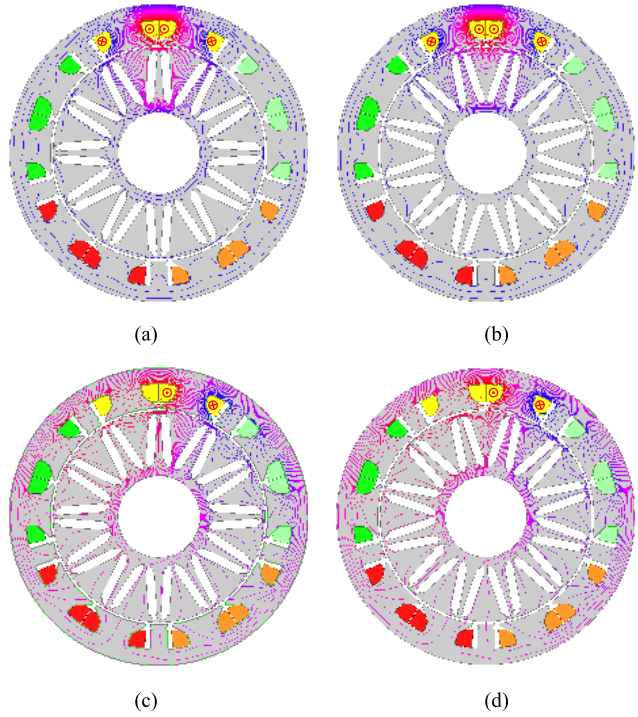


**FIGURE 4.** The flux lines distribution of five-phase FTPMSM with exciting current. Two sets of coils: (a) d-axis current and (b) q-axis current. Only one set of coils: (c) d-axis current and (d) q-axis current.

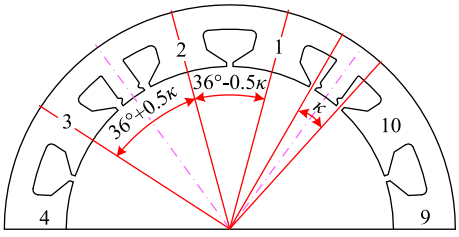


**FIGURE 5.** The stator structure of the five-phase FTPMSM.

$$k_{qv} = \cos v\left(\frac{36° - 3\kappa}{2}\right) = \cos v\left(18° - \frac{3\kappa}{2}\right) \tag{3}$$

$$k_{\mathrm{w}v} = k_{yv}k_{qv} = \left[\cos v\left(18° - \frac{3}{2}\kappa\right)\right]^2 \tag{4}$$

The variation diagrams of the winding coefficient with the small tooth angle under different harmonic orders are obtained by (4), and illustrated in Fig. 6. It can be figured out that with the increase of small tooth angle $\kappa$, the fundamental winding coefficient increases first. When $\kappa$ equals 12°, the fundamental winding coefficient reaches the maximum value 1, and then begins to decrease. At this angle, coil pitch is full-pitch, and the amplitude of fundamental EMF reaches the maximum. In order to enhance motor torque density, the small teeth angle of five-phase FTPMSM equals 12°.

### B. ANALYSIS AND DESIGN OF INDUCTANCE

The short-circuit fault may result in overcurrent. The magnetic field generated by the short-circuit current may cause

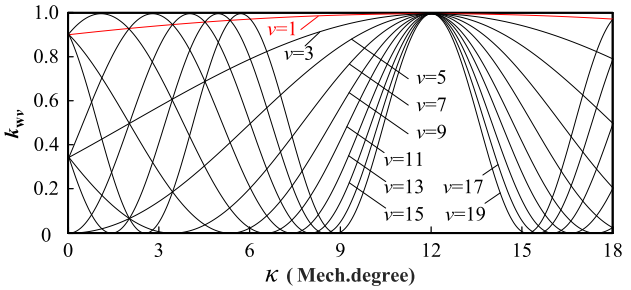


**FIGURE 6.** The variation diagram of the winding coefficient with the small teeth angle under different harmonic orders.

irreversible demagnetization of the PM. The steady-state short-circuit current is given by

$$I_s = \frac{E_0}{\sqrt{(\omega L)^2 + R^2}} = \frac{\psi_{PM}}{\sqrt{2}\sqrt{L^2 + (R/\omega)^2}} \tag{5}$$

where $I_s$ is the RMS of steady-state short-circuit current, $R$ is the phase resistance, $L$ is the phase inductance, $\omega$ is the electrical angular velocity, $E_0$ is the no-load back EMF, and $\psi_{PM}$ is the amplitude of PM flux.

Refer to (5), increasing the phase inductance of PMSM is the most effective way to reduce short-circuit current [18]. Since mutual inductance of the five-phase FTPMSM is almost zero, the inductance of each phase winding only contains self-inductance. The self-inductance consists of armature reaction inductance and leakage inductance. The inductance of the motor is given by

$$L = L_s = L_m + L_\sigma \tag{6}$$

where $L_s$ is the phase self-inductance, $L_m$ is the excitation inductance, and $L_\sigma$ is the leakage inductance.

Ignoring the effect of the interior PM on the reluctance of magnetic circuit, and assuming that the permeability of ferromagnetic material is infinite, the excitation inductance can be expressed as

$$L_m = \frac{\mu_0 l_{ef} N_c^2}{\delta}\left(\frac{2}{5}\pi D - 2b_0 - b_{st}\right) \tag{7}$$

where $\mu_0$ is the permeability of vacuum, $l_{ef}$ is the axial equivalent length of stator, $N_c$ is the number of coil turns, $\delta$ is the air-gap length, $D$ is the stator inner diameter, $b_0$ is the open width of slot, and $b_{st}$ is the width of small tooth.

The leakage inductance of PMSM includes slot leakage inductance and end winding leakage inductance. The five-phase FTPMSM adopts the structure of FSCW, thus the end winding is short and its leakage inductance is small. Therefore, slot leakage inductance is the main component of winding leakage inductance. Fig. 7 shows the stator slot shape. It can be figured out that the phase slot leakage inductance consists of the slot leakage inductance of the two coils in a big slot and the slot leakage inductance of two coils in two small slots, thus the slot leakage inductance $L_{\sigma s}$ can be

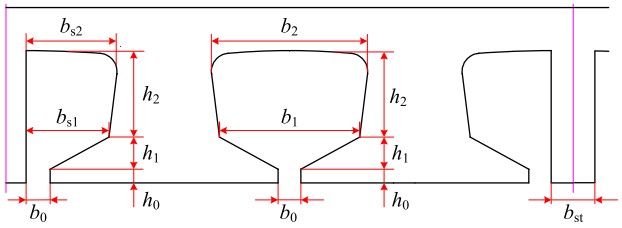


**FIGURE 7.** The stator slot shape.

expressed as

$$L_{\sigma S} = \mu_0 l_{ef} N_c^2 \left[4\left(\frac{2h_2}{3(b_1+b_2)} + \frac{2h_1}{b_0+b_1} + \frac{h_0}{b_0}\right) + 2\left(\frac{2h_2}{3(b_{s1}+b_{s2})} + \frac{2h_1}{b_0+b_{s1}} + \frac{h_0}{b_0}\right)\right] \tag{8}$$

where $h_x$ ($h_0$, $h_1$, $h_2$) and $b_x$ ($b_0$, $b_1$, $b_2$, $b_{s1}$, $b_{s2}$) are the parameters of the stator slot as shown in Fig. 7.

According to (7) and (8), the self-inductance is closely related to the dimensions of air-gap and slot. Using small air-gap, deep and narrow slot can increase the self-inductance and decrease the short-circuit current. Under the same condition of phase current, the reactance voltage is increased with the increase of inductance, which makes the converter VA rating larger. Considering that the increased inductance can effectively limit short-circuit current, the addition of converter VA rating is acceptable. The determination of stator slot size and air-gap length need to consider the inductance as well as the current density of the conductor, the flux density of the teeth and the stator yoke, and the torque density. In the optimization process of the air-gap length and stator slot size, set air-gap flux density, winding inductance, and preventing irreversible demagnetization of the PM under short-circuit fault as optimization indexes. In addition, the proposed motor has specific uses, and its weight and volume are clearly limited. The weight of the motor is not more than 26 kg, and the volume is restricted to 190mm × 190mm × 190mm. The optimization process is shown in Fig. 8.

### C. SELECTION OF ROTOR STRUCTURES

The rotor structure of PMSM affects magnetic circuit and applicable situation of the motor. Fig. 9 shows three different kinds of rotor structures commonly used in PMSM, where the arrow direction corresponds to the magnetizing direction of PM.

Fig. 9(a) shows the surface permanent magnet (SPM) rotor structure. This rotor structure can easily obtain approximate sinusoidal air-gap flux density waveform and low cogging torque through the optimization of PM shape and pole-arc coefficient. However, the PM is exposed in the air-gap, thus a large number of MMF harmonics caused by SPWM inverter supply will lead to eddy current loss in PM, and the loss will raise temperature of PM, which makes it at the risk of irreversible demagnetization. The winding inductance of PMSM with this rotor structure is small, thus the short-circuit current will be large, and the fault-tolerant capability is poor.

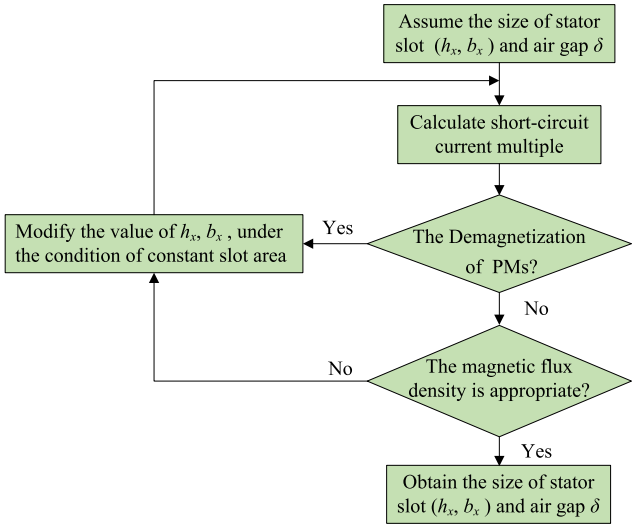


**FIGURE 8.** The optimization process of stator slot size and air gap length.

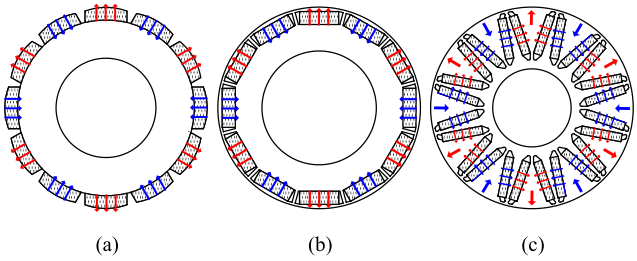


**FIGURE 9.** (a) SPM rotor structure. (b) IPM rotor structure with conventional type. (c) IPM rotor structure with V-shape.

In addition, the fixation of PM is also a challenge for the motor with high speed.

Fig. 9(b) and Fig. 9(c) show different IPM rotor structures of conventional type and V-shape, respectively. This kind of rotor structure has the advantages of simple structure, flux-weakening capability, wide constant-power speed range, reliable operation, and high mechanical strength. The PM is placed inside the rotor, which can reduce the influence of harmonic magnetic field on PM and lower PM eddy current loss. More importantly, this structure has small equivalent air-gap, which can improve the winding inductance and limit short-circuit current. Fig. 9(b) shows the conventional type of interior rotor structure, due to the five-phase FTPMSM has small rotor volume and large number of poles, the space for PM in this structure is not enough to obtain high air-gap flux density. Fig. 9(c) shows the interior rotor structure with V-shape, this rotor structure can enlarge the space for PM, thereby enhancing the air-gap flux density and increasing the torque density of the motor.

Fig. 10 shows the inductance waveforms of three motors, which have same stator and different rotor structures as shown in Fig. 9. It can be seen that the inductance of the motor with V-shape IPM rotor structure is the largest, followed by conventional type IPM rotor structure, and the SPM structure is the smallest. Fig. 11 shows the PM eddy current loss and

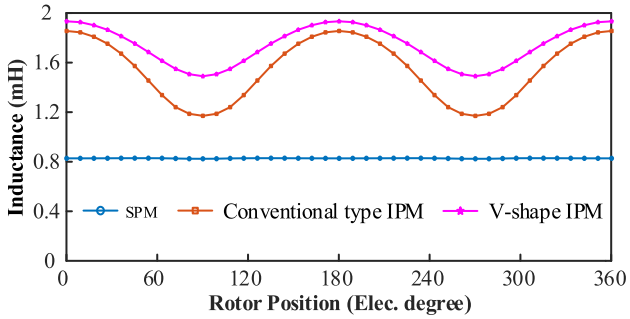


**FIGURE 10.** The inductance waveforms of three motors.

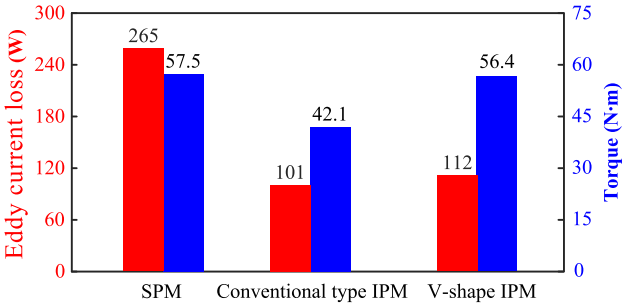


**FIGURE 11.** The PM eddy current loss and electromagnetic torque of three motors with rated current.

electromagnetic torque of three motors with rated current. It can be observed that the motor with V-shape rotor structure can meet both low PM eddy current loss and high power density compared with the others.

Based on the above analysis, in order to reduce the PM eddy current loss, limit short-circuit current, and increase the torque density of the motor, the five-phase FTPMSM adopts the rotor structure of IPM with V-shape as shown in Fig. 9(c).

## IV. FINITE ELEMENT ANALYSIS OF THE PROPOSED FTPMSM

### A. DIMENSIONS OF THE FTPMSM

The rated power of the five-phase FTPMSM is 20kW, and the rated speed is 3500r/min. The slot size and air-gap length are determined through the optimization process shown in Fig. 8, while the remaining parameters are obtained by minimizing the volume and weight of the motor, maximizing the efficiency and meeting the constraint of current density. The parameters and dimensions are shown in table 1.

### B. NO-LOAD CHARACTERISTIC ANALYSIS

The 2D FEA simulations of the five-phase FTPMSM are conducted by Ansys Maxwell. No-load magnetic circuit is shown in Fig. 12, including the flux density distribution and the flux lines distribution. It can be observed that since the designed stator teeth and yoke are wide, the flux density of them are relatively low and the value is about 1.35T, which can meet the requirement of low iron loss. Fig. 13(a) shows the no-load air-gap flux density of the motor, and the corresponding harmonic analysis result is given in Fig. 13(b). It can be seen

**TABLE 1. The parameters and dimension of the five-phase FTPMSM.**

| Symbol | Quantity |
|---|---|
| Rated power (kW) | 20 |
| Rated DC bus voltage (V) | 270 |
| Rated speed (r/min) | 3500 |
| Rated phase voltage (V) | 140 |
| Current density (A/mm$^2$) | 22.5 |
| Number of slots | 10 |
| Number of poles | 12 |
| Number of turns per coil | 18 |
| Core length (mm) | 110 |
| Lamination factor of stator (mm) | 0.95 |
| Outer diameter of stator (mm) | 175 |
| Inner diameter of stator (mm) | 127 |
| Outer diameter of rotor (mm) | 124 |
| Small teeth angle | 12° |
| Height of slot-$h_0$, $h_1$, $h_2$ (mm) | 1.5, 6.5, 7.5 |
| Width of slot-$b_0$, $b_1$, $b_2$, $b_{s0}$, $b_{s1}$, $b_{s2}$ (mm) | 2.5, 17.5, 20.5, 2.5,11,13 |
| Air gap length (mm) | 1.5 |
| Total Weight (kg) | 29 |
| Material of stator and rotor | B20AT1200 |
| Rated efficiency/ Rated power factor | 95.3% / 0.90 |
| Ambient temperature (℃) | -183 |

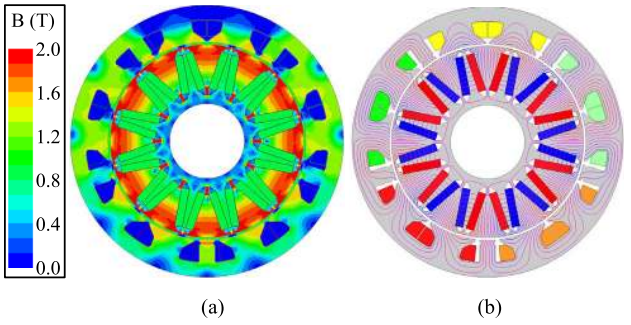


**FIGURE 12. No-load magnetic circuit of the five-phase FTPMSM. (a) The flux density distribution. (b) The flux lines distribution.**

that the 18 pole pairs harmonic component is large, making the synthetic air-gap flux density waveform approximate to flat-top wave, which improves the utilization of iron core. The fundamental amplitude can reach about 1.25T, which proves that the structure of IPM with V-shape can obtain high air-gap flux density.

Fig. 14(a) shows phase back EMF at rated speed. It can be illustrated that the back EMF waveform of each phase approximates to flat-top wave, and the phase difference of those between two adjacent phases is 72 electrical degrees. Fig. 14(b) shows the harmonic contents of back EMF based on harmonic analysis. It can be figured out that affected by the harmonic contents of air-gap flux density, the third harmonic is high, which is consistent with theory analysis.

Fig. 15 shows the winding inductances of phase A. It can be observed that the ratio of mutual inductance to self-inductance is 0.28%. Therefore, it is verified that the added small teeth can eliminate the electromagnetic coupling, which improves the fault-tolerant capability of the motor.

### C. LOAD CHARACTERISTIC ANALYSIS

Through the analysis of no-load characteristics, it is known that air-gap flux density owns more third harmonic

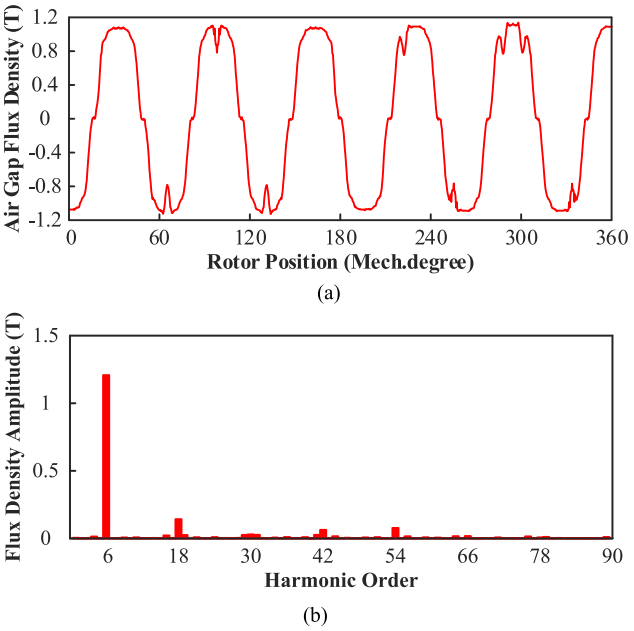


**FIGURE 13. (a) No-load air gap flux density. (b) Harmonic analysis of no-load flux density.**

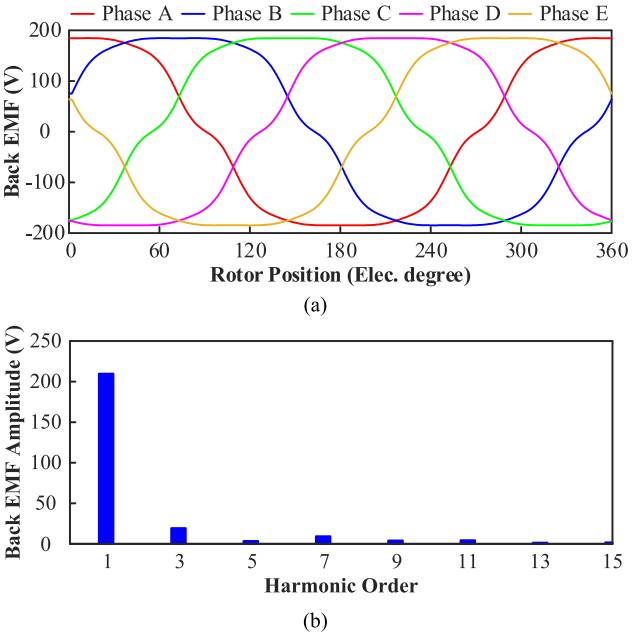


**FIGURE 14. (a) Phase back EMF. (b) Harmonic analysis of the phase back EMF.**

components. Therefore, the system performance can be improved by inputting appropriate third harmonic current [19]. Taking phase A current as example, the expression of that without the input of third harmonic current is as follow

$$i_A = I_m \cos \omega t = \sqrt{2} I \cos \omega t \tag{9}$$

where $I_m$ and $I$ are the amplitude and RMS of phase A current, respectively.

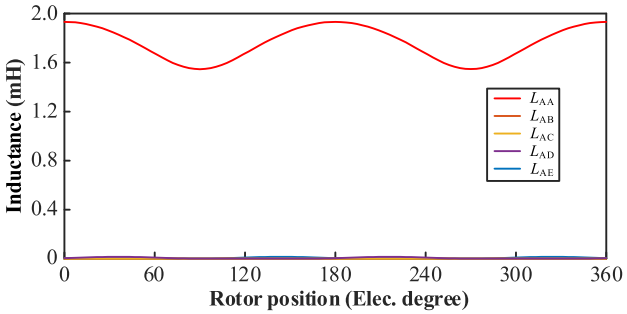


**FIGURE 15.** The winding inductances of phase A.

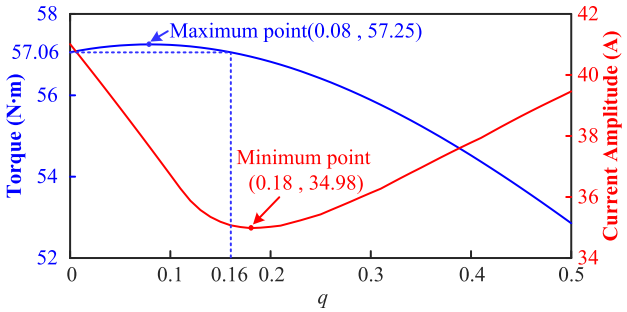


**FIGURE 16.** The electromagnetic torque and the current amplitude at different $q$.

When the third harmonic current is input, the phase A current can be expressed as

$$\begin{aligned} i_A &= i_{A1} + i_{A3} = I_{m1}\cos\omega t - I_{m3}\cos 3\omega t \\ &= \sqrt{2}I_1\cos\omega t - \sqrt{2}I_3\cos 3\omega t \end{aligned} \tag{10}$$

where $I_{m1}$ and $I_{m3}$ are the amplitudes of fundamental and third harmonic current, $I_1$ and $I_3$ are the correspondent RMS values. To ensure that the copper loss of the motor is constant, $I$, $I_1$, and $I_3$ should satisfy the following relationship

$$I_1^2 + I_3^2 = I^2 \tag{11}$$

Assuming the ratio of $I_3$ to $I_1$ is $q$, the relationship between $I_1$, $I_3$ can be expressed as

$$\begin{cases} I_3 = \dfrac{q}{\sqrt{1+q^2}}I \\ I_1 = \dfrac{1}{\sqrt{1+q^2}}I \end{cases} \tag{12}$$

The simulation is carried out under the condition that the motor phase current equals the rated current. Fig. 16 shows the electromagnetic torque and the current amplitude at different $q$. It can be seen that when $q$ equals 0, which means the third harmonic is not input, the electromagnetic torque is 57.06 N·m, and the current amplitude is 41.01 A. As $q$ increases, the electromagnetic torque increases first and then decreases, while the current amplitude decreases first and then increases. When $q$ equals 0.08, the electromagnetic torque reaches the maximum value of 57.25 N·m, which is increased by 0.33%. When $q > 0.16$, the electromagnetic torque is lower than the initial value. When $q$ equals 0.18, the current amplitude reaches the minimum value of 34.98 A,

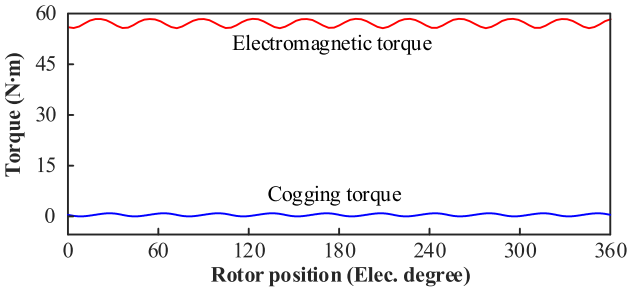


**FIGURE 17.** The waveforms of electromagnetic torque and cogging torque.

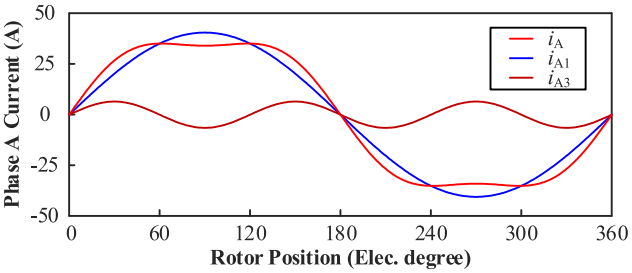


**FIGURE 18.** The current waveform when $q$ equals 0.16.

which is decreased by 14.7%. Therefore, the electromagnetic torque will be slightly increased by the input of an appropriate third harmonic current without changing the value of copper loss. At the same time, the current amplitude is significantly reduced, which is conducive to reducing the capacity of the inverter and the magnetic saturation of the stator core.

Taking account of high electromagnetic torque and low current amplitude, $q$ is taken as 0.16, i.e., $I_1 = 28.64$ A, $I_3 = 4.58$ A. Fig. 17 illustrates electromagnetic torque and cogging torque of the motor. It can be observed that the electromagnetic torque is 57.06 N·m and torque ripple is 2.1%. The amplitude of cogging torque is 0.6N·m, less than 1.1% of electromagnetic torque, which meets the requirements of motor design. Fig. 18 illustrates the current waveforms of the motor, it can be observed that the amplitude of current is 35.07 A, which is reduced by 14.5% of the initial value, and is beneficial to improve the performance of system.

Fig. 19 shows the flux density and the flux lines distribution of the motor with full load. It can be seen that the maximum flux density of yoke is 1.65T, and the flux density of stator teeth except a little part of tooth tip is less than 1.56T. Therefore, the flux density distribution of the motor with full load is reasonable. Fig. 20 shows efficiency map plot of the motor. It can be seen that the efficiency of the motor at rated condition is 95.3% and the motor has wide high efficiency area, which illustrates the proposed motor has high efficiency.

### D. FAULT-TOLERANT CAPABILITY

#### 1) OPEN-CIRCUIT FAULT

When stator winding open-circuit fault occurs, the synthesized current vector can be the same as that before the fault by changing the amplitude and phase of the remaining four healthy phase winding currents. In this way, fault-tolerant

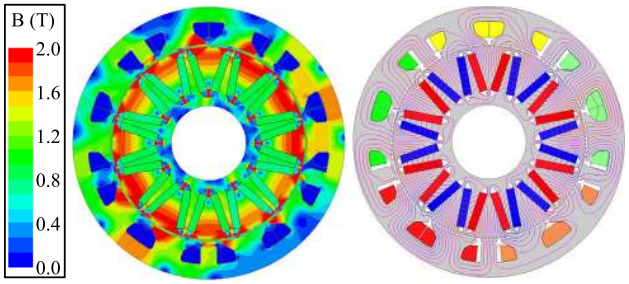


**FIGURE 19.** Full load magnetic circuit of the five-phase FTPMSM. (a) The flux density distribution. (b) The flux lines distribution.

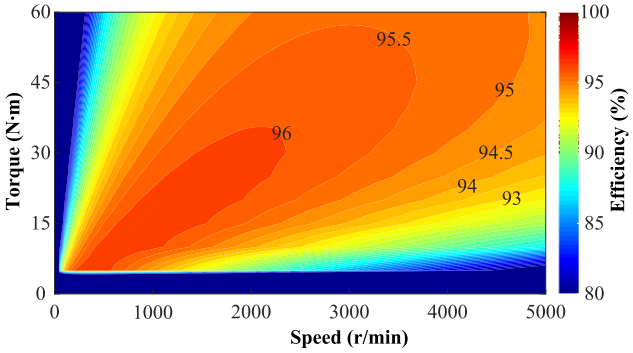


**FIGURE 20.** The efficiency map plot of the motor.

control (FTC) can be achieved [20], [21]. To make the FTC simple, third harmonic current will not be input into phase windings. Assuming phase A is open-circuit, the remaining four-phase currents under FTC are given by

$$\begin{cases} i_B = 1.382 I_m \cos(\omega t + \pi/5) \\ i_C = 1.382 I_m \cos(\omega t + 4\pi/5) \\ i_D = 1.382 I_m \cos(\omega t + 4\pi/5) \\ i_E = 1.382 I_m \cos(\omega t - \pi/5) \end{cases} \tag{13}$$

Fig. 21 shows the electromagnetic torque waveforms of the motor under normal condition, phase A open-circuit fault, and phase A open-circuit fault with FTC. It can be figured out that under normal condition, the electromagnetic torque is 57.06 N·m and the ripple is 2.1%. When open-circuit fault occurs in phase A, the electromagnetic torque of the motor without FTC is 45.46 N·m, and the ripple is 28.6%, compared with 55.93 N·m and 8.9% with FTC. As a consequence, the electromagnetic torque can be nearly the same as that before the fault by changing the amplitude and phase of the remaining four-phase currents under open-circuit fault condition. In this way, the five-phase FTPMSM can continue to operate under this fault.

In order to further verify the motor performance under open-circuit fault, two-phase open-circuit fault is analyzed, including two adjacent and non-adjacent phases open-circuit fault. Assuming two adjacent phases A and B are open-circuit, the remaining three-phase currents under FTC are

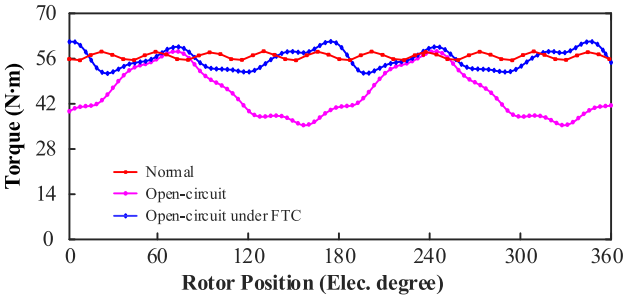


**FIGURE 21.** The torque waveforms under normal, phase A open-circuit fault, and phase A open-circuit fault under FTC.

given by

$$\begin{cases} i_C = 2.236 I_m \cos(\omega t - 2\pi/5) \\ i_D = 3.618 I_m \cos(\omega t + 4\pi/5) \\ i_E = 2.236 I_m \cos(\omega t) \end{cases} \tag{14}$$

Assuming two non-adjacent phases B and E are open-circuit, the remaining three-phase currents under FTC are given by

$$\begin{cases} i_A = 1.382 I_m \cos(\omega t) \\ i_C = 2.236 I_m \cos(\omega t - 3\pi/5) \\ i_D = 2.236 I_m \cos(\omega t + 3\pi/5) \end{cases} \tag{15}$$

Fig. 22 shows the electromagnetic torque waveforms of the motor under normal condition, two-phase open-circuit fault, and two-phase open-circuit fault with FTC. It can be figured out that under normal condition, the electromagnetic torque is 57.06 N·m and the ripple is 2.1%. When open-circuit fault occurs in phase A and phase B, the electromagnetic torque of the motor without FTC is 34.36 N·m, and the ripple is 23.06%, compared with 53.73 N·m and 12.7% with FTC. When open-circuit fault occurs in phase B and phase E, the electromagnetic torque of the motor without FTC is 33.91 N·m, and the ripple is 50.5%, compared with 54.53 N·m and 7.5% with FTC. The simulation results illustrate that the motor has high fault tolerance capability in two-phase open-circuit fault, especially in two non-adjacent phases open-circuit condition.

### 2) SHORT-CIRCUIT FAULT

When the PMSM has a short-circuit fault, there will be a large short-circuit current. The high temperature and magnetic field created by the short-circuit current will cause irreversible demagnetization of the PM. In order to reduce short-circuit current and improve the fault-tolerant capability, it is necessary to optimize rotor structure. Fig. 23 shows two models with the same stator. It can be figured out that in Fig. 23(a), a conventional SPM rotor structure is used, and in Fig. 23(b), a proposed V-shape IPM rotor structure is applied. In order to test the fault-tolerant capability of two structures under short-circuit fault, all phases of the motor are short-circuited. Fig. 24 shows the short-circuit currents of two models with different rotor structures. It can be figured out that the steady-state current RMS values of SPM and V-shape IPM rotor structures are 94.06 A and 54.58 A, respectively.

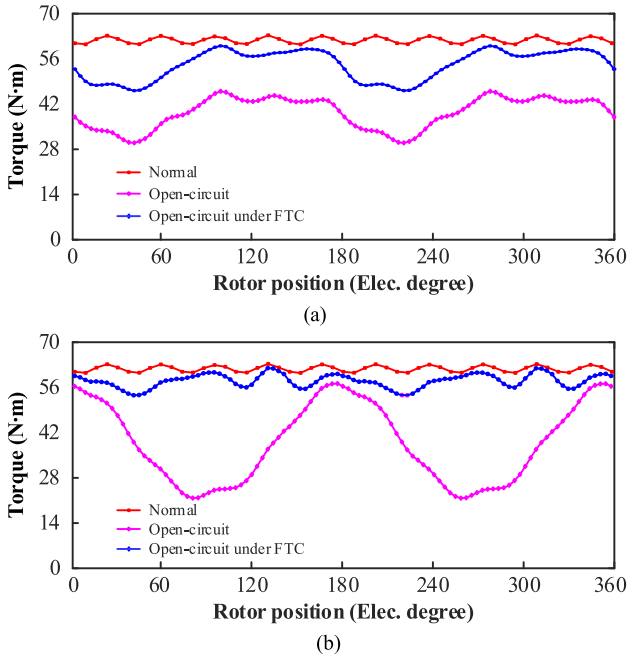


**FIGURE 22.** The torque waveforms under normal, two-phase open-circuit fault, and two-phase open-circuit fault with FTC. (a) Phase A and B open-circuit. (b) Phase B and E open-circuit.

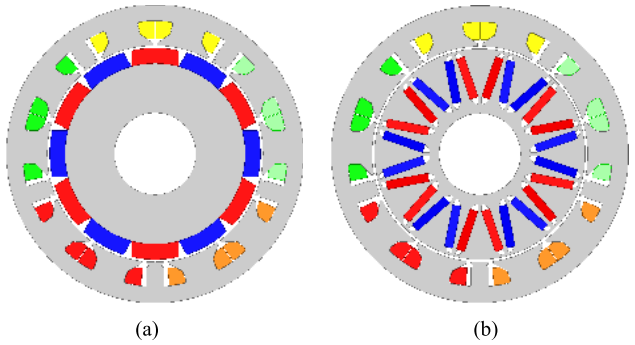


**FIGURE 23.** (a) Conventional SPM rotor structure. (b) Proposed V-shape IPM rotor structure.

Compared with conventional SPM rotor structure, the steady-state current RMS value of proposed V-shape IPM rotor structure is reduced by 42.0%. The simulation results show that the proposed rotor structure can effectively limit the short-circuit current.

Fig. 25 shows the magnetic field distribution of the motor under the condition that the short-circuit currents reach the steady state. It can be seen that when the five-phase FTPMSM has the most serious short-circuit fault, the remanence of the PM which is affected most seriously is 0.65T, so there is no irreversible demagnetization of the PM. Therefore, the motor with proposed rotor structure have strong fault-tolerant capability when short-circuit fault occurs.

## V. EXPERIMENTAL RESULTS ANALYSIS

In order to verify the theory analysis and simulations results, the prototype of the proposed five-phase FTPMSM is built as shown in Fig. 26.

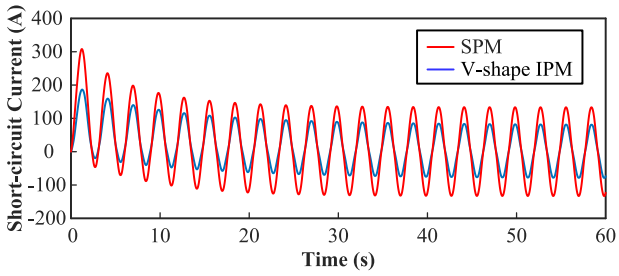


**FIGURE 24.** The short-circuit currents. (a) SPM. (b) V-shape IPM.

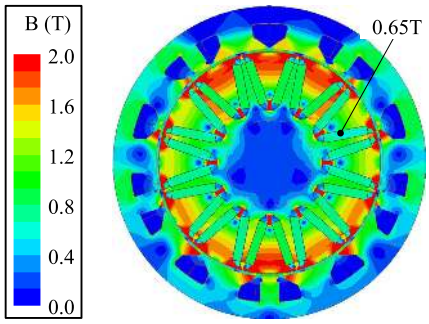


**FIGURE 25.** The magnetic field distribution of the motor with steady state short-circuit current.

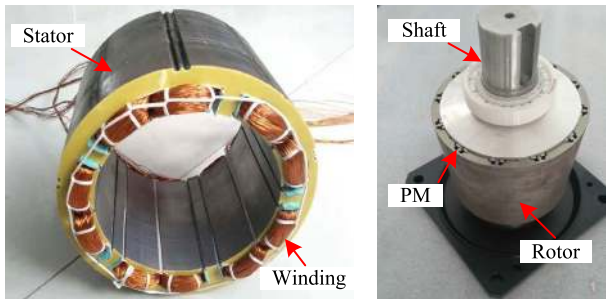


**FIGURE 26.** The prototype of the five-phase FTPMSM.

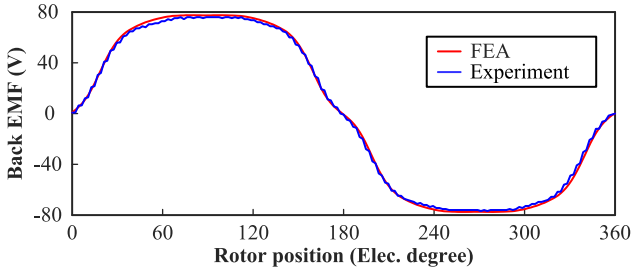


**FIGURE 27.** Phase back EMF under FEA and experiment.

Fig. 27 illustrates the experiment and simulation waveforms of phase back EMF at the speed of 1470 r/min, and the corresponding harmonic analysis are illustrated in Fig. 28. It can be observed that the experiment results agree with the simulation results, which verify the validity of design and theory analysis.

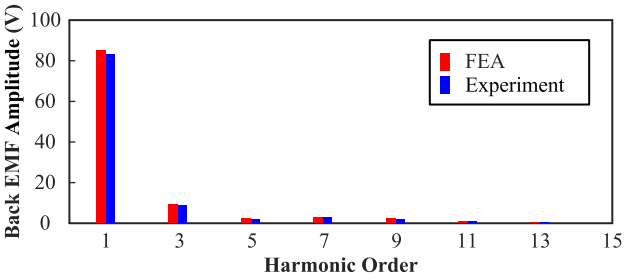


**FIGURE 28.** Harmonic analysis of phase back EMF under FEA and experiment.

## VI. CONCLUSION

A kind of five-phase FTPMSM applied in aerospace SG system is proposed in this paper. By theory analysis and FEA results, it is verified that the mutual inductance among different windings is eliminated as a result of small teeth in stator. Considering the motor will be used in a low temperature environment for a short time, the stator slot size is designed relatively small, and to increase its torque density, higher current density and air-gap flux density are adopted. Meanwhile, the stator teeth and yoke are designed wide to reduce iron loss. By using appropriate air-gap length and stator slot size, the self-inductance is increased, thus short-circuit current is decreased, and irreversible demagnetization of the PM is avoided when short-circuit fault occurs. Due to air-gap flux density with more third harmonic components, amplitude of currents is reduced by inputting appropriate third harmonic current into each phase. FEA method is applied to analyze its no-load and load characteristics as well as the fault-tolerant capability under open-circuit and short-circuit faults. Simulation results show that the proposed motor has good performance and superior fault-tolerant capability. Experiment results agree with the simulation, which verify the validity of design and theory analysis.

## REFERENCES


[1] B. Sarlioglu and C. T. Morris, "More electric aircraft: Review, challenges, and opportunities for commercial transport aircraft," *IEEE Trans. Transport. Electrific.*, vol. 1, no. 1, pp. 54–64, Jun. 2015.

[2] J. A. Rosero, J. A. Ortega, E. Aldabas, and L. Romeral, "Moving towards a more electric aircraft," *IEEE Aerosp. Electron. Syst. Mag.*, vol. 22, no. 3, pp. 3–9, Mar. 2007.

[3] S. Bozhko, S. S. Yeoh, F. Gao, and C. Hill, "Aircraft starter-generator system based on permanent-magnet machine fed by active front-end rectifier," in *Proc. 40th Annu. Conf. IEEE Ind. Electron. Soc.*, Dallas, TX, USA, Nov. 2014, pp. 2958–2964.

[4] E. Ganev, "Selecting the best electric machines for electrical power-generation systems: High-performance solutions for aerospace more electric architectures," *IEEE Electrific. Mag.*, vol. 2, no. 4, pp. 13–22, Dec. 2014.

[5] C. A. Ferreira, S. R. Jones, W. S. Heglund, and W. D. Jones, "Detailed design of a 30-kW switched reluctance starter/generator system for a gas turbine engine application," *IEEE Trans. Ind. Appl.*, vol. 31, no. 3, pp. 553–561, May 1995.

[6] A. K. Jain, S. Mathapati, V. T. Ranganathan, and V. Narayanan, "Integrated starter generator for 42-V powernet using induction machine and direct torque control technique," *IEEE Trans. Power Electron.*, vol. 21, no. 3, pp. 701–710, May 2006.

[7] N. Jiao, W. Liu, T. Meng, J. Peng, and S. Mao, "Detailed excitation control methods for two-phase brushless exciter of the wound-rotor synchronous starter/generator in the starting mode," *IEEE Trans. Ind. Appl.*, vol. 53, no. 1, pp. 115–123, Jan./Feb. 2017.

[8] A. M. El-Refaie, "Fractional-slot concentrated-windings synchronous permanent magnet machines: Opportunities and challenges," *IEEE Trans. Ind. Electron.*, vol. 57, no. 1, pp. 107–121, Jan. 2010.

[9] W. Cao, B. C. Mecrow, G. J. Atkinson, J. W. Bennett, and D. J. Atkinson, "Overview of electric motor technologies used for more electric aircraft (MEA)," *IEEE Trans. Ind. Electron.*, vol. 59, no. 9, pp. 3523–3531, Sep. 2012.

[10] J.-W. Jung, S.-H. Lee, G.-H. Lee, J.-P. Hong, D.-H. Lee, and K.-N. Kim, "Reduction design of vibration and noise in IPMSM type integrated starter and generator for HEV," *IEEE Trans. Magn.*, vol. 46, no. 6, pp. 2454–2457, Jun. 2010.

[11] C.-F. Wang, M.-J. Jin, J.-X. Shen, and C. Yuan, "A permanent magnet integrated starter generator for electric vehicle onboard range extender application," *IEEE Trans. Magn.*, vol. 48, no. 4, pp. 1625–1628, Apr. 2012.

[12] Y. Jiang, Z. Zhang, W. Jiang, W. Geng, and J. Huang, "Three-phase current injection method for mitigating turn-to-turn short-circuit fault in concentrated-winding permanent magnet aircraft starter generator," *IET Electr. Power Appl.*, vol. 12, no. 4, pp. 566–574, Apr. 2018.

[13] K. N. Pavithran, R. Parimelalagan, and M. R. Krishnamurthy, "Studies on inverter-fed five-phase induction motor drive," *IEEE Trans. Power Electron.*, vol. PEL-3, no. 2, pp. 224–235, Apr. 1988.

[14] E. Levi, "Multiphase electric machines for variable-speed applications," *IEEE Trans. Ind. Electron.*, vol. 55, no. 5, pp. 1893–1909, May 2008.

[15] Y. Chen and B. Zhang, "Minimization of the electromagnetic torque ripple caused by the coils inter-turn short circuit fault in dual-redundancy permanent magnet synchronous motors," *Energies*, vol. 10, no. 11, p. 1798, Nov. 2017.

[16] Y. Chen, X. Chen, and Y. Shen, "On-line detection of coil inter-turn short circuit faults in dual-redundancy permanent magnet synchronous motors," *Energies*, vol. 11, no. 3, p. 662, Mar. 2018.

[17] A. Wang, Y. Jia, and W. L. Soong, "Comparison of five topologies for an interior permanent-magnet machine for a hybrid electric vehicle," *IEEE Trans. Magn.*, vol. 47, no. 10, pp. 3606–3609, Oct. 2011.

[18] X. Jiang, W. Huang, R. Cao, Z. Hao, and W. Jiang, "Electric drive system of dual-winding fault-tolerant permanent-magnet motor for aerospace applications," *IEEE Trans. Ind. Electron.*, vol. 62, no. 12, pp. 7322–7330, Dec. 2015.

[19] L. Parsa and H. A. Toliyat, "Five-phase permanent-magnet motor drives," *IEEE Trans. Ind. Appl.*, vol. 41, no. 1, pp. 30–37, Jan./Feb. 2005.

[20] E. Levi, R. Bojoi, F. Profumo, H. A. Toliyat, and S. Williamson, "Multiphase induction motor drives—A technology status review," *IET Electr. Power Appl.*, vol. 1, no. 4, pp. 489–516, Jul. 2007.

[21] L. Parsa and H. A. Toliyat, "Fault-tolerant interior-permanent-magnet machines for hybrid electric vehicle applications," *IEEE Trans. Veh. Technol.*, vol. 56, no. 4, pp. 1546–1552, Jul. 2007.


**YIGUANG CHEN** received the B.S. degree in electrical engineering from the Hefei University of Technology, China, in 1984, the M.S. degree in electrical engineering from Tianjin University, China, in 1990, and the Ph.D. degree in electrical machines and apparatus from the Shenyang University of Technology, China, in 2008.

Since 2008, he has been a Professor with the Department of Electrical Engineering, School of Electrical and Information Engineering, Tianjin University. His research interests include the fault-tolerant design of electrical machines, motor fault diagnosis, motor for aerospace applications, and permanent magnet synchronous motor.

**BO LIU** received the B.S. degree in electrical engineering and automation from the China University of Mining and Technology, Xuzhou, China, in 2017. He is currently pursuing the M.S. degree in electrical engineering with the School of Electrical and Information Engineering, Tianjin University, Tianjin, China. His research interest includes the design and control of permanent magnet synchronous motor.